Scholar Publishing Group
Academic Journal of Environmental Biology
https://doi.org/10.38007/AJEB.2022.030201
ISSN 2789-8407 Vol. 3, Issue 2: 1-20

On-line Detection Method of Near-infrared Spectra of Greenhouse Gases in Mountain Forest Soil

Kazuyonshi Yoshiie*

University of Sydney, Australia

**corresponding author*

Keywords: Greenhouse Gases, Near Infrared Spectroscopy, Mountain Forest Soil, Online Detection System

Abstract: Mountain forest soil is an important source of global greenhouse gas emissions, including carbon dioxide (CO2), methane (CH4) and nitrogen oxide (N2O), but the current research on the impact of greenhouse gas emissions from mountain forest soil on the climate is very scarce. This article will focus on methane emissions from mountain forest soils for testing, and introduces a near-infrared spectroscopy on-line inspection, analysis and measurement method for greenhouse gases in mountain forest soils. In this paper, a photoelectric detection system is designed. Based on the STM32F103VB motherboard as the hardware foundation and wireless remote communication technology, a set of mountain forest soil greenhouse gas concentration detection system is developed to achieve online monitoring of mountain forest soil greenhouse gas emissions. The difficulty of this paper is mainly due to the low signal-to-noise signal of greenhouse gases in mountain forest soil. It is difficult to capture the signal. In order to improve performance and cost considerations, this paper uses a differential absorption detection method. The experimental results in this paper show that the full-scale accuracy is 0.6% FS, the system response time is less than 16s, and the relative standard deviation is 1.41%. It has good repeatability and stability, which proves that the system meets the design requirements. At the end of this paper, a brief analysis of the source of the system error is also provided, which provides a direction for further improving the accuracy of the system.

1. Introduction

At present, the main problems of the global climate are caused by global warming caused by greenhouse gas emissions, and then the soil layer is an important source of atmospheric greenhouse gases. 80% to 90% of N_2O and 30% of CH_4 in the atmosphere are derived from soil . And the carbon content of terrestrial ecosystems is mainly provided by forest ecosystems, of which 73% of the carbon elements in the global soil system are forest soil systems. Therefore, it is an important

component that affects the changes in global greenhouse gas emissions.

In recent years, few people have focused on the detection of CH_4 gas released from soil as the focus of research, because in the intuitive sense of scholars, CH_4 emissions in mountain forest soil are very small, and the impact on the greenhouse effect is not as significant as CO_2. However, the relative capacity of CH_4 to affect climate change is 21 to 23 times that of CO_2, and the impact rate on the greenhouse effect accounts for about 15% of all greenhouse gases [1-2].

In order to explore the process of greenhouse gases produced by soil physical factors in the soil, Guggenberger G proposed a new model relationship and found that they have complex and close interactions, showing that in many cases, the physical conditions of the soil may be to control emission levels The main factor [3]. Wang B studied the relationship between soil and greenhouse gas emissions under the global warming environment. Using the new calculation system to calculate new discoveries, he found that in the late succession system, due to a large amount of methane oxidation, the global warming change level and reached an advanced level. This shows that reducing the soil system can effectively reduce methane emissions and thus reduce the chance of global warming [4]. In order to study the impact of greenhouse gas emissions from mountain soils on the global climate, Zhibin LIN proposed the climatedition.net model. This model is as effective as other state-of-the-art climate models, but the climate sensitivity ranges from less than 2 K to more than 11 K. Wait. This suggests that models with this extreme sensitivity are essential for studying the various possible responses of the climate system to rising greenhouse gas levels, as well as assessing the risks associated with specific targets to stabilize these levels [5-6].

The main work of this paper is as follows: (1) Introduce the research background and ingenious significance of near-infrared spectroscopy detection of greenhouse gases in mountain forest soil, explain the principle of near-infrared spectroscopy in detail, explore the principle of near-infrared spectroscopy absorption methane detection and differential absorption detection technology The theory derives the relationship between concentration and detector output voltage. (2) The overall system design plan and ideas are put forward, and the hardware design and software design of the methane monitoring system are completed, including the optical path system and the circuit system. (3) Design the calibration laboratory platform, and complete the system calibration experiment and system performance verification experiment in the laboratory environment. Through the mountain forest soil monitoring experiment and analysis of the experimental data, it is proved that the system meets the expected design requirements.

2.Proposed Method

2.1 Methane Gas Detection Technology

At present, there are many methods for the detection of Jiaxiao gas, and each method has its own advantages, disadvantages and application range due to the different detection mechanism. According to the detection principle, it can be divided into catalytic combustion, heat conduction, light interference, infrared absorption and other methods and detection methods based on other principles. The following is an introduction to these different detection methods.

(1) Catalytic combustion method

Catalytic combustion type detection principle: the catalytic combustion reaction (oxidation) of methane burns on the components coated with catalytic substances, releases the reaction heat, the heat released by the combustion of different concentrations of methane burning gas is different, and the temperature of the component will change its resistance Change, by measuring the resistance change value to get the actual concentration of methane. The catalytic combustion method is the

most common and effective and reliable method for measuring low concentration (usually in the lower explosion limit range of 0 to 4%) in practical applications. After more than half a century of use and development, the catalytic combustion method has reached a certain level. Its power consumption is getting lower and lower, and its performance is getting higher and higher. A burn sensor based on this principle has certain advantages, such as high sensitivity, short response time, low cost, simple structure and easy to use, and is not easily interfered by environmental factors such as temperature and humidity. However, the characteristics of this sensor must be accompanied by a series of problems, such as short life span, short measurement range, and easy poisoning. In addition, there is no way to suppress the zero drift and sensitivity drift of the sensor [7-8].

(2) Heat conduction method

The principle of thermal conductivity detection: according to the difference in thermal conductivity of different gases, and the gas concentration is different, the thermal conductivity is also different, this feature is measured by constructing a bridge to measure the change in resistance of the detection element to measure the concentration of formazan. The sensor made by the principle of heat conduction method has good stability when the gas concentration to be measured is high, and the sensitivity is not high when the gas concentration is low. Therefore, it is often used in the detection of high concentration forty-nine burns in the range of 4% to 100%. Generally, in order to obtain a full-range A-Hang sensor, the thermal conductivity A-anti-sensor can be combined with the catalytic combustion A-Huan sensor [9]. The thermal conductivity armor sensor circuit is simple and easy to use, there is no poisoning, and the life is long, but the signal obtained by the thermal conductivity armor sensor is weak and there is a zero drift, and it is sensitive to gases with thermal conductivity different from air, and the detection error is poor. Larger [10].

(3) Optical interference method

Detection principle of optical interference method: The difference in the propagation speed of light in air and nail burning will cause the optical path difference, causing the interference fringes to move. The concentration of the nail courtyard is measured by measuring the amount of interference fringe movement. The optical interference principle has been widely used for the detection of forging burns after more than half a century of development. Its advantages are also obvious. It has the characteristics of high accuracy, excellent stability, and wide detection range. But there are also the following deficiencies:

It is easily affected by the gas environment. When the oxygen content in the air is low and the nitrogen-oxygen ratio is unbalanced, the measurement error is large: it is easily interfered by other gases and the selectivity is poor [11].

(4) Near infrared spectroscopy

The principle of near-infrared spectroscopy: when the infrared light beam passes through Jiaxiao gas, the output light intensity will change due to infrared absorption, and the concentration of formazan is measured by detecting the amount of change in light intensity. It can be known from the selective absorption of molecules that any kind of gas molecule has its own absorption spectrum. Only when the emission spectrum of the light source overlaps with the absorption spectrum of the gas molecule, the spectrum absorption phenomenon occurs, which leads to the weakening of the light intensity [12-13]. The intensity of light absorbed has a certain relationship with the concentration of the gas to be measured, and the concentration of the gas to be measured can be obtained by calculation by detecting the input and output intensity of light of a specific wavelength.

Near-infrared spectral absorption detection technology is the result of long-term development of spectral analysis technology. In the past, the spectrum analysis technology was only used for gas analysis in the laboratory, and it was gradually applied to the detection of gas concentration. The

technology is relatively mature. The mainstream methane sensors on the market are based on this detection technology. The burn sensor based on infrared absorption principle has many advantages, and the detection range is relatively wide: it has good stability and high accuracy; it is not easy to be interfered by other gases, has good selectivity, fast response, not easy to be poisoned and aging, and has a long life It is also a major advantage [14-15].

2.2 Basic Theory of Near Infrared Spectroscopy

(1) Ideal harmonic oscillator model

In molecules, according to quantum theory, there are electronic energy levels and vibration-rotational energy levels in molecules. When the transition between the electronic energy level and the vibration-rotation energy level occurs, a molecular absorption spectrum and a molecular emission spectrum are generated, which are shown as band spectra.

Transitions between different energy levels of molecules produce different molecular absorption or emission spectra. The vibration energy level interval is generally 0.05-1eV, and the electromagnetic spectrum generated by the vibration energy level transition is in the mid-infrared spectrum region. Light has wave-particle duality. According to quantum theory, when infrared light of a specific wavelength meets a molecule, if the light does not interact with the molecule, the light then passes through the substance without generating an absorption spectrum; if the light interacts with the molecule in a specific way, the substance absorbs the wavelength The light produces an absorption spectrum, which is called infrared activity [16].

A diatomic infrared active molecule will be used as an example for description. Think of the active molecules of diatomic molecules as vibrating dipoles. The dipole vibrates at a specific frequency and amplitude. The atoms at both ends of the dipole are regarded as protons with masses m1 and m2, respectively, and the chemical bond is regarded as a massless spring. The model is shown in Figure 1 [17].

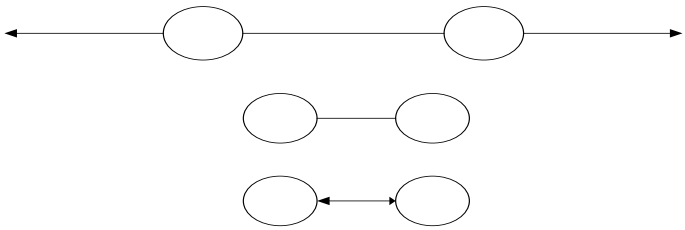

Figure 1. Infrared active molecular dipole model

Here, the vibration frequency of the dipole is ν, and the maximum distance between two atoms when the chemical bond vibrates is called the resonance amplitude. When the frequency of the incident photon matches the vibrational frequency of the molecule, the molecule absorbs the energy of the photon and increases the amplitude of the dipole, but the vibrational frequency is constant [18].

The dipole vibration model is also called the harmonic oscillator model. The resonance frequency depends on the force constant of the chemical bond and the mass of the atoms at both ends of the chemical bond. The total energy of the harmonic oscillator is proportional to the frequency of vibration. Applying Hooke's law, the vibration frequency of the harmonic oscillator is expressed as:

$$v = \frac{1}{2\pi}\sqrt{\frac{k}{\left(\frac{1}{m_1}+\frac{1}{m_2}\right)}} \quad (1)$$

Where: K: chemical bond force constant, different chemical bonds have different force constants m_1 and m_2: the atomic mass of atoms 1 and 2 can be derived from formula (1), if you know the chemical bond force constant, you can find a specific chemical bond The stretching vibration frequency. Conversely, the force constant of a specific chemical bond can be obtained from the vibration frequency of the molecular vibration spectrum. The force constant of a single bond is about one-half of that of a double bond and one-third of that of a triple bond. And as the atomic mass increases, the resonance frequency will decrease.

The study of quantum mechanics shows that the chemical bond cannot be simply regarded as a massless spring. The vibration energy of the chemical bond in the molecule is quantized, that is, the molecule can be at different vibration energy levels. Quite a lot [19-20]. In an ideal situation, polyatoms can be viewed as a series of independent diatomic harmonic oscillators, so that the energy of polyatomic molecules can be expressed as follows:

$$\mathrm{E}(v1, v2, v3.....) = \sum_{i=1}^{3N-6}(V_i + \frac{1}{2})hv_i \quad (2)$$

Where: h: Planck constant

ν: chemical bond vibration frequency

V: Vibration quantum number, V = 0, 1, 2, 3 ...

(2) Non-resonance

In fact, when the particle is close to a certain degree, the true compression force is limited by the spring itself. When the spring is extended, the spring will deform when it is stretched to a certain extent, and it cannot be restored to its original shape. The curve of potential energy change of the ideal harmonic oscillator model is shown as the parabola shown in B in Figure 2.

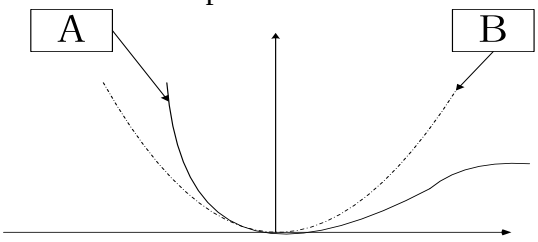

Figure 2. Potential energy curve of diatomic molecules

In the molecule, there is a potential energy barrier because the electron cloud of the two bonded atoms hinders the approach of the nucleus during the process of decreasing the vibration amplitude. In the process of increasing vibration amplitude, if the vibration energy level reaches the dissociation energy, the chemical bond will eventually break. The curve A in Figure 2 illustrates this situation. As the interatomic distance decreases, the potential energy increases rapidly. As the interatomic distance increases, the potential energy gradually approaches zero [21].

As shown by A in Figure 2, for non-harmonic oscillators, the energy level spacing is non-uniform. As the energy increases, the energy level gradually approaches. The energy of the

non-harmonic oscillator is expressed by the following formula:

$$E_v = (V + \frac{1}{2})h\nu - (V + \frac{1}{2})^2 Xh\nu + ... \quad (3)$$

$$\nu = \frac{1}{2\pi}\sqrt{\frac{k}{\left(\frac{1}{m_1} + \frac{1}{m_2}\right)}}$$

In the formula: , Representing the fundamental frequency

X: non-resonance constant

K: force constant of chemical bond (single bond 5N / cm, double bond 10N / cm, triple bond 15N / cm)

And， m_1, m_2: atomic mass.

The position of the band obtained by equation (3) is closer to the actual position of the band. In practice, the position of the frequency-doubling absorption band of a fundamental frequency absorption spectrum band can be calculated by formula (4), where the displacement due to non-resonance is about 1% to 5%.

$$\lambda = \frac{\lambda_1}{k} + \lambda_1(0.01,0.02,...,0.05) \quad (4)$$

In the formula: k: represents the frequency multiplier

λ_1: position of the fundamental frequency absorption band.

For the position of the fundamental frequency absorption band at 3800 nm, the position of its first frequency-doubling absorption band is in the range of $\frac{3800}{2} + 3800 * 0.01 = 1938m$ to $\frac{3800}{2} + 3800 * 0.05 = 2090m$ .Therefore, there are many different vibration energy levels in the molecule, and these energy levels usually contain two or more vibration forms with similar vibration energy levels. This situation is called energy level degeneration. At this time, Fermi resonance will occur, which will enrich the near-infrared spectral characteristics, but may also lead to misinterpretation of the spectrum. When a Fermi resonance occurs, one frequency increases due to the mutual repulsion of energy levels, while the other frequency decreases. This repulsion depends on the inharmonicity of the energy levels at which the interaction occurs. The stronger the inharmonicity, the stronger the Fermi resonance will be [22].

(3) Absorption spectrum analysis of molecular fundamental frequency, frequency doubling and combined frequency

Since the frequency of molecular vibration includes the fundamental frequency, multiples of frequencies at various levels, and various combined frequencies, the molecule may absorb the corresponding electromagnetic wave of the same frequency in the environment through resonance absorption (the amplitude of the internal vibration of the molecule changes), which is the basis of the molecule Frequency absorption, frequency doubling absorption and combined frequency absorption [23].

The transition of the molecule from the vibrational ground state to the first excited state is called the fundamental frequency transition, and the absorption of radiation generated by this transition is

the fundamental frequency absorption. Since the selection rule of the ideal harmonic oscillator when transitioning between different energy levels is ΔV=±1, that is, ideally, the transition can only occur between adjacent energy levels [24].

In fact, due to the existence of non-resonance, the selection rule of the transition will also appear ΔE=±1, ±2……, in addition to the fundamental frequency, it can also occur from the ground state to the second or higher excited state (V = 2 , 3, ...). This kind of transition is called second-order frequency doubling or multi-stage frequency-doubling transition, and the resulting absorption band is second-order frequency doubling or multi-stage frequency doubling absorption, which is collectively called frequency-doubling absorption.

Polyatomic molecular vibration is a linear synthesis of many simple independent vibrations. Because various vibrations are not strictly harmonic, they may interact with each other. If the electromagnetic wave photon energy is exactly equal to the energy required for a certain two fundamental frequency transitions , And these two fundamental frequency vibrations have the same symmetry, then a photon of this energy may simultaneously excite two fundamental frequency transitions. The wave number (or frequency) of the absorption peak appearing in the spectrum is equal to the sum of the two fundamental frequency vibration wave numbers (or frequency), and this absorption is called combined frequency absorption.

The absorption of molecules in the mid-infrared spectrum is due to the transition between the adjacent vibration energy levels of the vibration state, that is, the fundamental frequency absorption; and the absorption in the near-infrared spectrum is due to the frequency doubling or combined frequency absorption of molecular vibrations As a result, this is the source of information in the near infrared spectrum.

Because the near infrared region starts from 4000 cm^{-1} to 12500 cm^{-1}, the fundamental frequency of the group is below 2000 cm^{-1}[25]. The frequency of the first-order octave and the combined frequency of the spectral region is less than 4000 cm^{-1}, so it is not in the near infrared region , these groups can only enter the near-infrared region with higher-order frequency doubling and combining frequencies, but the intensity is very weak, so the information contained in the near-infrared spectrum region is mainly the information of certain groups with a fundamental frequency above 2000 cm^{-1} . Because the absorption strength of the hydrogen-containing groups is high, the practical significance in the near-infrared analysis is mainly the characteristic groups mainly containing H-containing groups (including OH, NH, CH, etc.), as shown in Table 1.

Table 1. The approximate position of the combined frequency of the main groups and the absorption bands of frequency doubling at all levels

Unit	cm^{-1}				nm			
Group	C-H	N-H	O-H	H_2O	C-H	N-H	O-H	H_2O
Combined frequency	4250	4650	5000	5155	2350	2150	2000	1940
Double frequency	5800	6670	7000	6940	1720	1500	1430	1440
Triple frequency	6500	9520	10500	10420	1180	1050	950	960
Quadruple	11100	12500	13500	13330	900	800	740	750
Octave	13300				750			

In terms of the distribution of absorption intensity, the absorption intensity of each frequencydoubling and combined frequency of organic matter in the near-infrared spectrum region is approximately one order of magnitude higher than the fundamental frequency or the previous frequency doubling. Take the absorption intensity of the CH bond as an example, see the table 2. The absorption intensity from the combined frequency to the frequency doubling at all levels is getting lower and lower. Each time the frequency doubling increases about one level, the relative absorption intensity decreases by about an order of magnitude.

Table 2. Distribution of C-H group frequency doubling in the near infrared region

	Wavelength range/nm	Relative absorption
Group	2900~3200	1
Combined frequency	2200~2450	0.01
Double frequency	1600~1800	0.01
Triple frequency	1150~1250	0.001
Quadruple	850~940	0.0001
Octave	700~780	0.00005

(4) Factors affecting the near-infrared spectrum

In some special cases, certain factors may interfere with the near-infrared spectrum of the substance and change the position of the absorption band . These factors mainly have the following aspects:

1) Association between molecules. The asymmetric distribution of the electron and proton charges in the molecule will cause a strong electrostatic field, which exerts an influence on neighboring molecules. The result of such intermolecular interactions is association, and the strongly acting molecular clusters show significant interference, the most common being hydrogen bonding. This type of bond is extremely sensitive to temperature. There are two extreme cases that stem from this interaction. One is that the strength of this interaction is comparable to ordinary covalent bonds, thereby forming binary or polyvalent compounds. The other is that the original covalent bond is completely broken to cause ionization. This type can happen both inside and between molecules [26].

2) Changes in the state of matter. A change in the state of a substance will cause a change in the degree of freedom of the substance molecule, which will cause a change in the absorption band.

3) Temperature factor. Not only does temperature change affect the association of molecules, but the number of excited molecules is a function of temperature, which follows the Boltzmann factor. So temperature will affect the absorption of light by molecules.

4) Electronegative factors. In some compounds, halogen and H are connected to the same carbon atom, which will affect the position and intensity of the adjacent C-H absorption band. The reason lies in the electronegativity of halogen.

5) Fermi resonance. There are many Fermi resonance absorption bands in the near infrared spectrum. When the non-interfering frequencies of two kinds of the same kind of vibration are close, resonance will occur between the two kinds of vibration. When resonance occurs, the frequency and intensity of both absorption bands change, but they are still separated. If the two resonance absorptions are very close, the intensity of the absorption band is roughly the average of the intensity of the band when it is not disturbed. If the two resonance absorption bands are far apart, the intensity of the weak absorption band will obviously increase when resonance occurs, but the

position of the band will hardly change.

2.3 Lambert-Beer Law

(1) Contents of Lambert-Beer Law

The theoretical basis for quantitative analysis of infrared absorption spectroscopy is Lambert-Beer 's Law .

Lambert's law states that the proportion of light absorbed by a transparent medium has nothing to do with the intensity of incident light; each equal thickness of the medium absorbs the same proportion of light in the optical path.

Beer's law states that the amount of light absorbed is proportional to the number of molecules that produce light absorption in the optical path.

The combination of the two laws, known as Lambert-Beer Law, can be regarded as a macroscopic representation of the above molecular vibration principle. For a mixed medium containing n kinds of material components, the complete mathematical expression is:

$$A = \ln(I_0 / I_t) = \ln(1/T) = \sum_n A_n(\lambda) = \sum_n \alpha_n(\lambda) C_n L \quad (5)$$

Where: A: absorbance as a function of wavelength

I_0: incident radiation intensity

I_t: transmitted radiation intensity

Cn: the concentration of component n (mg / d L)

L: optical path length (m)

α_n: Absorption coefficient of component n (mg / dL.m)

T: Transmittance = It / I0

For the absorption coefficient α, it is the inherent property of the substance itself. Experiments show that the same substance with different concentrations has the same absorption coefficient at the same wavenumber; different substances have different absorbance coefficients at different wavenumbers.

(2) The conditions for the establishment of Lambert-Beer law

The establishment of Lambert-Beer law requires certain conditions as prerequisites, mainly in the following five aspects:

1) There is no interaction between substances in the absorption process, but the absorbance of each substance is additive;

2) During the absorption process, the temperature of the substance remains unchanged;

3) The role of radiation and matter is limited to the absorption process, without chemical phenomena such as fluorescence and scattered light;

4) Absorbent is a continuous system with uniform distribution;

5) The absorbance reading should be within the linear range of the standard curve, otherwise it will have a greater impact on the accuracy of the result. Assuming that a single substance absorbs a single wavelength, equation (5) can be changed to:

$$\ln T = -\alpha CL$$
$$\frac{\Delta T}{T} = -\alpha \Delta CL \tag{6}$$
$$\frac{\Delta C}{C} = \frac{\Delta T}{T \ln T}$$

Let $\Delta T = 1$, which means that the transmittance changes by 1 unit. Under different transmittances, the deviation of the calculation result is shown in Table 3:

Table 3. Transmittance and concentration error correspondence table

T(%)	$\Delta C / C$(%)	T(%)	$\Delta C / C$(%)
95	-20.52	36.8	-2.72
90	-10.55	30	-2.77
80	-5.60	20	-3.11
70	-4.01	10	-4.34
60	-3.26	5	-6.88
50	-2.89	3	-9.51
40	-2.73	2	-12.78

It can be seen from Table 3 that when the transmittance is between 20% and 60%, the density error caused by the error of the detection result is less, and the density error caused by the greater or smaller transmittance is larger.

2.4 Gas Absorption Spectrum

(1) CO_2 gas absorption spectrum

Carbon dioxide gas has absorption bands with different absorption strengths in the near-infrared and mid-infrared bands. The strong absorption bands are distributed in 2.7μm, 4.3μm and 11.4μm, and the weak absorption bands are mainly distributed in 1.4μm, 1.6μm and 2.0μm.

Carbon dioxide gas has absorption bands with different absorption strengths in the near-infrared and mid-infrared bands. The strong absorption bands are distributed in2.7μm, 4.3μm and 11.4μm, and the weak absorption bands are mainly distributed in 1.4μm, 1.6μm and 2.0μm.

In the near infrared band, two absorption bands of 1580nm and 1600nm are commonly used. In this band, the loss of the optical fiber is low, and long-distance optical fiber gas detection can be achieved. In this paper, the carbon dioxide gas absorption line at 1580 nm is selected for detection, and the absorption spectrum of carbon dioxide gas in this band is found in the standard spectrum database (HITRAN).

It can be seen from the figure that there are two absorption envelopes of CO_2 gas near 1580nm, there are more than 40 strong absorption lines, and the absorption intensity of the strongest absorption line is1.76*10-23 cm^{-1} / (molecule·cm^{-2}), the corresponding absorption wavelength is 1572.4nm.

After calculation of the standard CO_2 gas absorption line, it can be obtained that the half-width of the absorption peak of CO_2 gas is about 0.035nm; in the band of 1570nm-1575nm, the CO_2 gas absorption line basically exhibits a periodic distribution, between each two absorption lines It is about 0.32nm apart.

(2) CH_4 gas absorption spectrum

In the near infrared region, there are many pan-band and combined bands. In 1983, Tohoku University of Japan used InGaAsPLED and a germanium detector to measure the ν2 + 2ν3 combined band. The Q branch band absorption around 1.33μm is quite strong, and its absorption peak appears at 1.3312μm. In 1984, the university also tested the 2ν3 harmonic band of the CH_4 molecule and found that the spectral bandwidth of the Q-band near 1.66 μm is about 3 nm, and the maximum absorption wavelength is at 1.6654 μm .

The C H4 molecule has 4 inherent vibrations, corresponding to 4 fundamental frequencies, all in the mid-infrared band. The wave numbers of the four fundamental frequencies are:ν1＝ 2913.0 c m －1 ,ν2＝1533.3 c m－1 ,ν3＝3018.9 c m－1 ,ν4＝1305.9 c m－1 Each natural vibration corresponds to a spectral absorption band, and their wavelengths are 3.43, 6.53, 3, 31, 7.66μm.

3. Experiments

3.1 System Design Scheme Design

The overall structure of the system is composed of methane sensor detection system, data acquisition terminal and monitoring software on the server. System design can be divided into hardware design and software design. The system hardware is mainly divided into two parts, the optical path system and the circuit system. The optical path system includes infrared light source, detector and gas absorption gas chamber: the circuit system mainly includes the core controller STM32 minimum system circuit, power supply module, light source drive and modulation module, signal conditioning circuit module (amplifier, filter circuit), temperature sensing Modules and other peripheral interface circuits (real-time clock, data storage, serial communication and other modules); the system also integrates a GPRS communication module for remote wireless transmission of collected data.

The system is powered by an independent power module. The microprocessor generates PWM waves to control the driver to modulate the light source. The infrared light emitted by the infrared light source passes through the gas chamber containing the gas to be measured. After the gas is fully absorbed, the selective transmission of the filter is used After the end to the detector. The detector converts it into two voltage signals according to the received light intensity. The two voltage signals are very weak when output by the detector, and need to be pre-amplified and filtered by the microprocessor ADC peripherals; the system uses a low-power 32-bit ARM processor STM32F103VB as the main control chip, and leads to the standard The JTAG interface is convenient for programming and debugging of the program; the real-time clock (RTC) module of the STM32 controller provides a time basis for timing data collection and real-time storage. Use the SPI interface of the STM32 controller to write the collected data and time into the SD card synchronously to achieve local storage backup to prevent data incompleteness caused by the loss of GPRS signal. In addition, the system uploads the collected data to the cloud server in real time through the GPRS module through the RS232 interface. The monitoring center software is developed on the server, which is responsible for establishing connection communication with the GPRS module, and analyzing and storing the received data packets. Finally, the data can be displayed through the constructed WEB dynamic webpage to access the database.

3.2 System Calibration Scheme Design

(1) Design of calibration experiment platform

In order to carry out system calibration and system testing, a calibration experiment platform was built in the laboratory environment. The experiment platform consisted of pure nitrogen, standard methane gas of different concentrations, gas pressure reducing valve, precision rotameter, methane monitoring system and host computer software Module composition. The structure of the calibration experiment platform is shown in Figure 3.

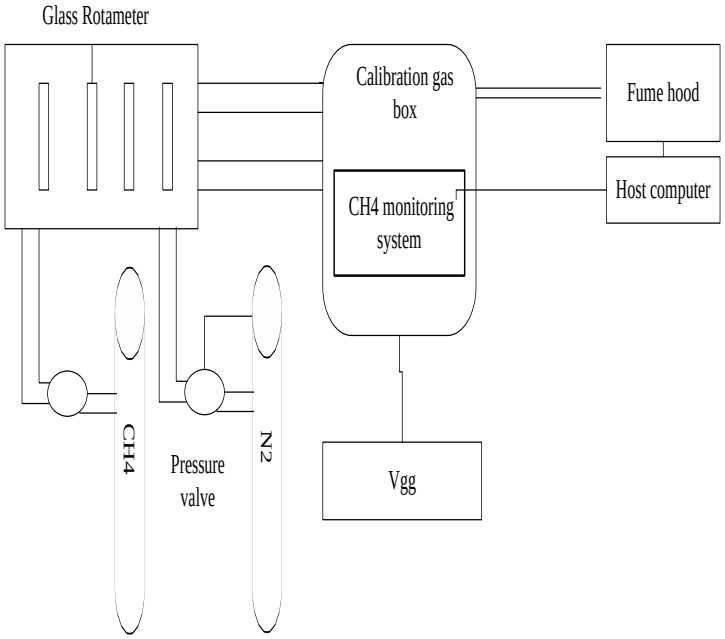

Figure 3.Structure diagram of calibration experiment platform

(2) Prototype and experimental device

Before calibration, prototypes and experimental devices need to be prepared. The laboratory has a bottle of pure N2 and 1%, 2%, and 3% concentration of CH_4. According to the calibration principle, the more data points are calibrated to the system, the smaller the segmentation, the better the system accuracy.Therefore, this design will use the existing calibration experiment platform, use pure N_2 to dilute the existing standard methane gas to obtain more concentration of CH_4 gas, and achieve the calibration of the system at 5% interval concentration.

3.3 Calibration Experiment

The system calibration experiment is mainly divided into a zero-point calibration experiment. The calibration experiment is to obtain the corresponding relationship between the system output and the concentration of formazan, and then solidify the correspondence to the STM32. The actual concentration of the nail salon can be calculated by measuring the output voltage of the sensor. The calibration experiment steps are:

(1) Build the calibration platform according to the above, at standard atmospheric pressure and normal temperature, fill the gas box with pure nitrogen, exhaust the air, and turn on the machine. After the data is stable, read the 4.1 measurement channel output V_{gas0} and the reference channel output V_{ref0} , Get $K_0 = V_{gas0} / V_{ref0}$.

(2) The methane gas of different concentration is introduced into the gas box at a constant flow rate, and the monitoring result of the monitoring system is observed through the software of the host

computer. The ratio $F = V_{gas} / V_{ref.}$

(3) According to the data obtained from the gas absorption experiment, make a C-F graph, linearly fit by the least squares method, draw the fitting formula and solidify it into the STM32 microprocessor.

4. Discussion

4.1 Zero Calibration Experiment

Under standard atmospheric pressure and normal temperature, open the valve of the cylinder and fine-tune the pressure relief valve to purge the gas box with pure nitrogen at a constant flow rate. After the system is stable, the zero adjustment is completed, and the concentration corresponding to the output voltage of the system is 0. At this time, it is considered that the dual-channel output value of the detector reflects the light energy when infrared light of different wavelengths is not absorbed by the gas, and the dual-channel output is compared to obtain K_0. The experimental data of system zero calibration is shown in Table 4.

Table 4. Zero calibration experiment data

Num	Vgas0（V）	Vref0（V）	$K_0 = V_{gas0} / V_{ref0}$
1	2.175	1.849	1.170
2	2.154	1.830	1.170
3	2.205	1.980	1.170

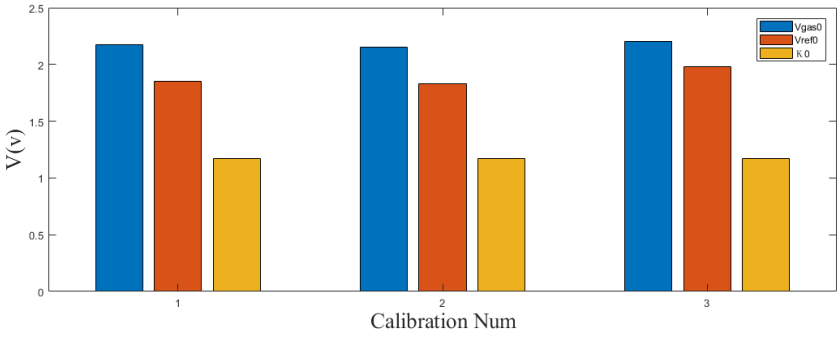

Figure 4. Zero calibration experiment data

It can be found from Figure 4 that K_0 can fully reflect its accuracy. And it is found from Fig. 4 that K_0 can fully represent the stability of the calibration data of the device.

4.2 Gas Absorption Experiment

Under the same environment of system zero calibration, use the experimental calibration platform to perform absorption experiments on the monitoring system under different concentrations of methane at 0.2%, 0.3%, 0.4%, 0.5%, 1%, 1.5%, 2%, 2.4%, and 3%. Record the output voltage V_{gas} of the system measurement channel and the output voltage V_{ref} of the reference

channel for each concentration separately. Table 5 shows the experimental data of methane burning gas absorption.

Table 5. Gas absorption experiment data

C（%）	V_{gas}（V）	V_{ref}（V）	$F=V_{gas}/V_{ref}$
0.2	2.083	1.824	1.121
0.3	2.054	1.844	1.136
0.4	2.064	1.873	1.104
0.5	2.053	1.878	1.105
1	2.612	1.832	1.045
1.5	1.980	1.854	1.071
2	1.930	1.878	1.022
2.4	1.768	1.886	1.004
3	1.346	1.775	0.976

The relationship between the output voltage of the measurement channel and the reference channel and the concentration of formazan according to the gas absorption experiment is shown in Figure 5. It can be seen from the figure that the measurement channel exhibits a weakening of the light intensity due to the absorption of near-infrared light at the wavelength by the formazan gas, and the output voltage value is smaller as the concentration of formazan increases. The near infrared radiation has no absorption effect, and its output value is basically unchanged, which is in line with the principle of near infrared absorption and Lambert's law.

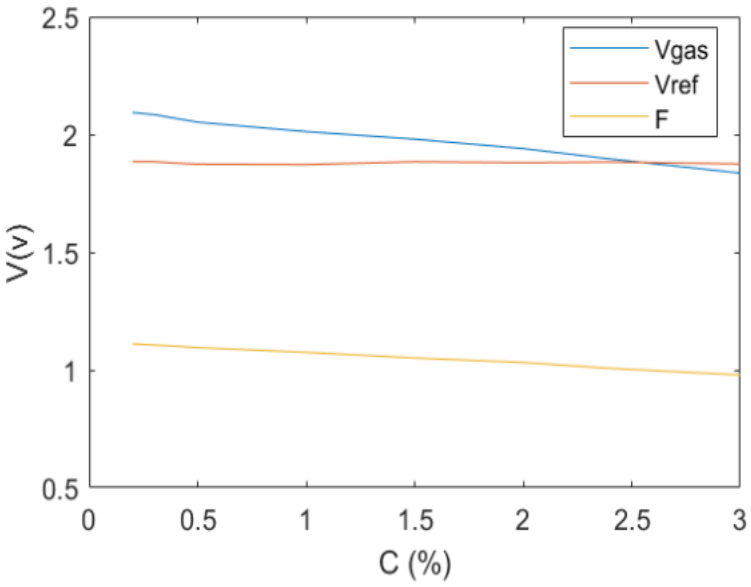

Figure 5. Relationship between output voltage and methane concentration

Figure 5 shows the C-F relationship diagram of the relationship between the dual-channel output ratio F (relative absorption rate) and methane concentration after the difference. Compared with the relationship between the measurement channel and methane concentration in Figure 5, the C-F relationship is better linear. Because the optical device is disturbed by environmental factors, the

relationship between the measurement channel and the methane concentration does not fully conform to the linearity of the theoretical derivation, and through differential detection, the linearity of the C-F relationship is improved, indicating that differential detection can reduce interference and improve system detection accuracy.

According to the C-F relationship, the C-F relationship is obtained by least-squares linear fitting:

$$y = -21.51768x + 24.10443 \tag{7}$$

Among them, y represents the relative absorption rate of gas F, X represents the gas concentration, burn (7) into the STM32 microprocessor, and then you can use the system to detect different concentrations of methane.

4.3 System Performance Verification Experiment

After the system calibration, in order to check the system performance, inversion experiments were carried out. The system is analyzed experimentally on accuracy, repeatability and stability. The experimental results show that the system has good accuracy, good stability and good repeatability, and meets the design requirements.

(1) Precision analysis

Under standard atmospheric pressure and normal temperature, put the calibrated and solidified system into the gas box, and pass 1%, 2%, and 3% methane gas into the gas box at a constant flow rate to measure the concentration value of the system output. And record the system response time (the time required for the system to reach 90% of the final value). The accuracy analysis experiment results are shown in Table 6.

Table 6. Precision analysis experiment results

Standard CH_4 concentration(%)	Measured CH_4concentration(%)	Corresponding time(%)
1	1.02	15
2	2.03	16
3	3.02	15

According to the above table, calculate the full-scale accuracy according to formula (8):

$$\frac{max|C_m - C_s|}{R} \times 100\% \tag{8}$$

Among them, Cm represents the measured methane concentration, and Cs represents the standard methane concentration. R is the full-scale value. The range of this design system is 0 ~ 5%, so R is 5%. The system full-scale accuracy calculated from Table 6 data and formula (8) is ±0.6% FS, and the system response time is not greater than 16S.

(2) Repeatable experiment

Under the same conditions as the calibration environment, the same measured object is measured multiple times in succession, and the degree of consistency of the measurement results is called repeatability. The relative standard deviation of the measurement results is usually used to characterize the repeatability of the system. First purge the air box with pure nitrogen for 10 minutes, and exhaust the air until the system shows "0". Then pass the standard methane gas with a concentration of 1% into the gas tank. When the system indication is basically stable, record the

measurement result C_i. Repeat the above steps 10 times under the same conditions. The experimental results are shown in Table 7. Finally, according to the experimental results, calculate the standard deviation and relative standard deviation.

The relative standard deviation is:

$$\sigma = \sqrt{\left(\sum_{i=1}^{n=10} \left(C_i - \bar{C} \right)^2 / (n-1) \right)}$$
$$\frac{\sigma}{\bar{C}} \times 100\% \approx 1.41\% \quad (9)$$

In the formula, C_i is the i-th measurement result, $\bar{C}$ the average value of n measurement results, n indicates the number of measurements n should be as large as possible, usually not less than 10.

After calculation: σ = 0.014283, the relative standard deviation is: 1.41%, indicating that the system has good repeatability.

Table 7. Repeatable experimental data

Test Num	Indication(%)	Avg(%)	Std	Relative Std(%)
1	1.02	1.034	0.014437	1.51
2	1.05			
3	1.07			
4	1.09			
5	1.13			
6	1.05			
7	1.04			
8	0.98			
9	1.05			
10	1.07			

(3) Stability experiment

Stability is a very important technical indicator to evaluate the performance of the system, and it indicates the ability of the system to maintain its display value constant for a long time. As the system monitors the trace methane emissions in the forest and mountain soil environment, the methane concentration after the gas tank enrichment is below 1%. Therefore, this paper conducted a system stability test on three groups of methane gas (0.4%, 0.6%, 0.8%) with different concentrations in the range of 0 ~ 1% (V / V). The test duration of each group is 5 days (720 * 10min), and data is collected every 10min. The experimental results are shown in Figure 6. (A) (b) (c) were 0.4%, 0.6%, 0.8% concentration test. The experimental results show that the measurement errors of different concentrations of methane gas are less than 0.01% (V / V), and the monitoring system has high monitoring accuracy and good stability.

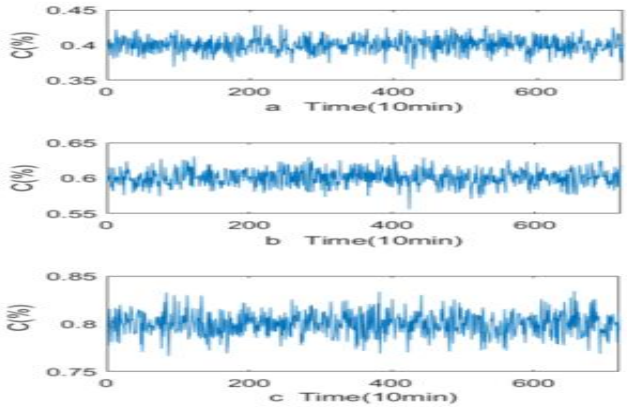

Figure 6. Stability experiment results

(4) Monitoring experiment and analysis

Since the concentration of formic acid enriched in the gas box in a short period of time did not change much, the experiment used intermittent monitoring and collected every 30 minutes. The device starts the acquisition work every hour and half point, and after completion, it will disconnect the power supply of the sensing device and the DTU wireless transmission unit through the relay, and at the same time, the controller enters the low power consumption mode to reach the lowest power consumption of the system. The experimental results are shown in Figure 7.

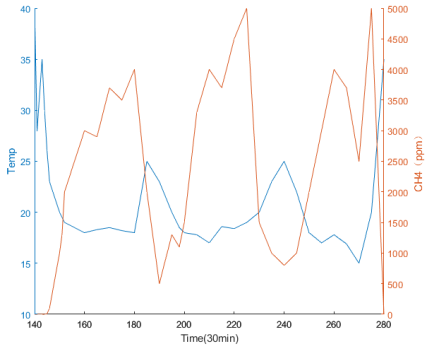

Figure 7.The law of methane concentration and temperature with time

The red line in Figure 7 represents the monitoring concentration of the AA, reflecting its emission flux. First of all, it gradually rises, which is shown as methane emissions, and then gradually declines, which is shown as the absorption of nail resistance; the blue line in the figure is the soil temperature, which changes with the change of air temperature: the methane monitoring concentration and soil temperature have obvious daily changes, It also shows that the monitoring concentration of methane has a significant negative correlation with soil temperature.

5. Conclusions

This paper designs a calibration experiment platform for the mountain forest soil greenhouse gas detection system. First, the system was calibrated, including zero-point calibration and gas absorption experiments. The least squares method was used to fit the experimental data to determine the system output voltage and methane concentration. Relationship, and burn this

relationship into the system. Secondly, the verification experiment and analysis of the system accuracy, repeatability and stability are made. The experimental results show that the full-scale accuracy is $\pm 0.6\%$, the system response time is not more than 16s, and the relative standard deviation is 1.41%, which has good repeatability and stability. Later, through field data analysis of mountain forest soil experiments, it was proved that the system met the expected design requirements.

In this paper, when using Lambert's law to derive the gas concentration, it is assumed that the monochromatic light is absorbed by the gas and then detected after reaching the detector. In fact, the near-infrared light passing through the filter is not a monochromatic light, but a bandwidth $\Delta\lambda = 0.03\mu m$, the center wavelength is the spectral band of the absorption wavelength, and at the same time, there is some stray light through the filter, which will cause certain errors. The error is called the Lambert deviation.

At the end of this paper, a brief analysis of the source of the system error is also provided, which provides a direction for further improving the accuracy of the system. From the above system performance verification experiment, the system designed has certain accuracy and stability to meet certain detection needs. However, there are some deficiencies and there is still some room for improvement.

References

[1] Zhijie Chen, Heikki Setälä, Shicong Geng. Nitrogen addition impacts on the emissions of greenhouse gases depending on the forest type: a case study in Changbai Mountain, Northeast China. Journal of Soils & Sediments, 2017, 17(1):23-34. https://doi.org/10.1007/s11368-016-1481-7

[2] Víctor Manuel Ruíz-Valdiviezo, Ángel Aguilar-Chávez, María del Rosario Cárdenas Aquino. Greenhouse gas emissions from a soil cultivated with wheat (Triticum spp. L.) and amended with castor bean (Ricinus communis L.) or Jatropha curcas L. seed cake: A greenhouse experiment. Plant Soil & Environment, 2018, 59(No. 12):556-561. https://doi.org/10.17221/368/2013-PSE

[3] Guggenberger G , Ludwig B , Menon M . Smith, K.A. Ball, T. Conen, F. Dobbie, K.E. Massheder, J. & Rey, A. 2003. Exchange of greenhouse gases between soil and atmosphere: interactions of soil physical factors and biological processes. European Journal of Soil Science. european journal of soil science, 2018, 54(4):779-791. https://doi.org/10.1046/j.1351-0754.2003.0567.x

[4] Wang, B, Lerdau, M, He, YL. Widespread production of nonmicrobial greenhouse gases in soils. Global Change Biology, 2017, 23(1):4472-4482. https://doi.org/10.1111/gcb.13753

[5] Zhibin LIN, Qi LIU, Gang LIU. Effects of Different Biochars on Pinus elliottii Growth, N Use Efficiency, Soil N 2 O and CH 4 Emissions and C Storage in a Subtropical Area of China. Pedosphere, 2017, 27(2):248-261. https://doi.org/10.1016/S1002-0160(17)60314-X

[6] Michael M. Loranty, Benjamin W. Abbott, Daan Blok. Reviews and syntheses: Changing ecosystem influences on soil thermal regimes in northern high-latitude permafrost regions. Biogeosciences Discussions, 2018:1-56.

[7] Zhao, Hong, Sun, Binfeng, Lu, Fei. Meta analysis on impacts of biochar on trace greenhouse gases emissions from staple crops in China. Transactions of the Chinese Society of Agricultural Engineering, 2017, 33(19):10-16.

[8] Xuming Wang, Min jie Hu, Hongchang Ren. Seasonal variations of nitrous oxide fluxes and soil

denitrification rates in subtropical freshwater and brackish tidal marshes of the Min River estuary. Science of the Total Environment, 2018, 616-617:1404-1413. https://doi.org/10.1016/j.scitotenv.2017.10.175

[9] L. Florentino-Madiedo, E. Díaz-Faes, R. García. Influence of binder type on greenhouse gases and PAHs from the pyrolysis of biomass briquettes. Fuel Processing Technology, 2018, 171:330-338. https://doi.org/10.1016/j.fuproc.2017.11.029

[10] María-Teresa Sánchez, Irina Torres, María-José de la Haba. Rapid, simultaneous, and in situ authentication and quality assessment of intact bell peppers using near-infrared spectroscopy technology.. Journal of the Science of Food & Agriculture, 2019, 99:págs. 1613-1622. https://doi.org/10.1002/jsfa.9342

[11] Marie Dumont, Laurent Arnaud, Ghislain Picard. In situ continuous visible and near-infrared spectroscopy of an alpine snowpack. Cryosphere, 2017, 11(3):1091-1110. https://doi.org/10.5194/tc-11-1091-2017

[12] Huang C J, Sun C W, Chou P H, et al. Functional connectivity during phonemic and semantic verbal fluency test: a multi-channel near infrared spectroscopy study (Conference Presentation). IEEE Journal of Selected Topics in Quantum Electronics, 2016, 22(3):43-48. https://doi.org/10.1109/JSTQE.2015.2503318

[13] QIU JUN, WANG YUNBAI, FU QIUJUAN. Rapid Determination of Calcium in Tobacco with Near Infrared Spectroscopy. Tobacco Science & Technology, 2017, 50(9):15-22.

[14] Plomgaard A M, Oeveren W V, Petersen T H, et al. The SafeBoosC II randomised trial: treatment guided by near-infrared spectroscopy reduces cerebral hypoxia without changing early biomarkers of brain injury. Pediatric Research, 2016, 79(4):528-535. https://doi.org/10.1038/pr.2015.266

[15] Ohlin L, Bazin P, Thibault-Starzyk F, et al. Adsorption of CO2, CH4, and H2O in Zeolite ZSM-5 Studied Using In Situ ATR-FTIR Spectroscopy. Journal of Physical Chemistry C, 2018, 117(33):16972–16982. https://doi.org/10.1021/jp4037183

[16] Ana Ledo, Marta Aguar, Antonio Núñez-Ramiro. Abdominal Near-Infrared Spectroscopy Detects Low Mesenteric Perfusion Early in Preterm Infants with Hemodynamic Significant Ductus Arteriosus. Neonatology, 2017, 112(3):238-245. https://doi.org/10.1159/000475933

[17] Stefan Heschl, Waltraud Bruchelt, Corinna Binder-Heschl. Near-infrared spectroscopy measures extinction of light by chromophores. European Journal of Anaesthesiology, 2019, 36(6):468-469. https://doi.org/10.1097/EJA.0000000000001010

[18] Joshi, A, Raigond, P, Singh, B. Near-infrared spectroscopy: a non-destructive tool for processing quality evaluation of potatoes. Indian Journal of Plant Physiology, 2017, 22(2):258-262. https://doi.org/10.1007/s40502-017-0291-2

[19] Carmella Vizza, William E. West, Stuart E. Jones. Regulators of coastal wetland methane production and responses to simulated global change. Biogeosciences, 2017, 14(2):431-446. https://doi.org/10.5194/bg-14-431-2017

[20] K. Andreassen, Alun Hubbard, M. Winsborrow. Massive blow-out craters formed by hydrate-controlled methane expulsion from the Arctic seafloor. Science, 2017, 356(6341):948-953. https://doi.org/10.1126/science.aal4500

[21] Williams S R O, Chaves A V, Deighton M H, et al. Influence of feeding supplements of almond hulls and ensiled citrus pulp on the milk production, milk composition, and methane emissions of dairy cows. Journal of Dairy Science, 2018, 101(3):2072-2083. https://doi.org/10.3168/jds.2017-13440

[22] Karel Castro-Morales, Thomas Kleinen, Sonja Kaiser. Year-round simulated methane

emissions from a permafrost ecosystem in Northeast Siberia. Biogeosciences Discussions, 2018, 15(9):2691-2722. https://doi.org/10.5194/bg-15-2691-2018

[23] Xiaoyuan Zhao, Yang Cao, Hongrui Li. Sc promoted and aerogel confined Ni catalysts for coking-resistant dry reforming of methane. Rsc Advances, 2017, 7(8):4735-4745. https://doi.org/10.1039/C6RA27266E

[24] Cunbao Deng, Xiaobo Wang, Yafei Shan, Zhiqiang Song. Study on the effect of low molecular hydrocarbon compounds on coal spontaneous combustion. Fuel,2022, 318,123193, https://doi.org/10.1016/j.fuel.2022.123193.

[25] Ali N. Ebrahimi. Mechanistic modeling of microbial interactions at pore to profile scale resolve methane emission dynamics from permafrost soil. Journal of Geophysical Research, 2017, 122(5):1216-1238. https://doi.org/10.1002/2016JG003674

[26] H. Chen, Z. Wang, X. Xu, S. Gong and Y. Zhou, The molecular behavior of pyridinium/imidazolium based ionic liquids and toluene binary systems, Phys. Chem. Chem. Phys., 2021, 23, 13300–13309 https://doi.org/10.1039/D1CP00874A